

# Algorithms for Poisson Phase Retrieval

Zongyu Li *Student Member, IEEE*, Kenneth Lange and Jeffrey A. Fessler *Fellow, IEEE*

**Abstract**—This paper discusses algorithms for phase retrieval where the measurements follow independent Poisson distributions, using maximum likelihood (ML) estimation. To optimize the log-likelihood for the Poisson phase retrieval model, we developed and compared several algorithms including Wirtinger flow (WF), Gerchberg Saxton (GS), majorize minimize (MM) and alternating direction method of multipliers (ADMM). Simulation results using random Gaussian sensing matrix, discrete Fourier transform (DFT) matrix and an empirical transmission matrix under Poisson measurement noise demonstrated that algorithms based on the Poisson model consistently produced higher quality reconstructions than algorithms (WF, GS) derived from Gaussian noise models when applied to such data. Moreover, the reconstruction quality can be further improved by adding regularizers that exploit assumed properties of the latent signal/image, such as sparsity of finite differences (anisotropic total variation) or of the coefficients of a discrete wavelet transform.

**Index Terms**—Poisson Phase retrieval, nonconvex optimization.

## I. INTRODUCTION

Phase retrieval is an inverse problem that has many applications in engineering and applied physics [1, 2], including radar [3], X-ray crystallography [4], astronomical imaging [5] and speech processing [6], where the goal is to recover the signal from only the magnitude of linear measurements, such as the magnitude of its Fourier transform [7]. This paper focuses on cases where the measurements follow Poisson distributions.

In most previous works, the measurement vector  $\mathbf{y} \in \mathbb{R}^M$  was assumed to have statistically independent elements following Gaussian distributions:

$$y_i \sim \mathcal{N}(|\mathbf{a}'_i \mathbf{x}|^2 + b_i, \sigma^2), \quad (1)$$

where  $\mathbf{a}'_i \in \mathbb{C}^N$  denotes the  $i$ th row of the system matrix  $\mathbf{A} \in \mathbb{C}^{M \times N}$ ,  $\mathbf{x} \in \mathbb{C}^N$  denotes the true unknown signal,

Zongyu Li and Jeffrey A. Fessler are with Department of Electrical Engineering and Computer Science, University of Michigan, Ann Arbor, MI 48109-2122 (e-mail: zonyul@umich.edu, fessler@umich.edu).

Kenneth Lange is with Departments of Computational Medicine, Human Genetics, and Statistics, University of California, Los Angeles, CA 90095 (e-mail: klange@ucla.edu).

Research supported in part by USPHS grants GM53275 and HG006139, and by NSF Grant IIS 1838179. Code for reproducing the results will be available on <https://github.com/ZongyuLi-umich> after the paper is accepted.

and  $b_i$  denotes a known mean background signal for the  $i$ th measurement, where  $i = 1, \dots, M$ . For this Gaussian noise model, the ML estimate of  $\mathbf{x}$  corresponds to the following nonconvex optimization problem

$$\hat{\mathbf{x}} = \underset{\mathbf{x} \in \mathbb{C}^N}{\operatorname{argmin}} g(\mathbf{x}), \quad g(\mathbf{x}) \triangleq \sum_i |y_i - b_i - |\mathbf{a}'_i \mathbf{x}|^2|^2. \quad (2)$$

To solve (2), numerous algorithms have been proposed, such as Wirtinger Flow [8], Gerchberg Saxton [9] and majorize-minimize (MM) methods [7].

However, in some low-photon count applications [10–15], a Poisson noise model is more appropriate:

$$y_i \sim \operatorname{Poisson}(|\mathbf{a}'_i \mathbf{x}|^2 + b_i), \quad (3)$$

where here  $b_i \geq 0$  denotes known mean background counts for the  $i$ th measurement, e.g., as arising from dark current [16]. The optimization problem for ML estimation under the Poisson model (3) is:

$$\hat{\mathbf{x}} = \underset{\mathbf{x} \in \mathbb{C}^N}{\operatorname{argmin}} f(\mathbf{x}), \quad f(\mathbf{x}) \triangleq \sum_i \psi(\mathbf{a}'_i \mathbf{x}; y_i, b_i),$$

$$\psi(v; y, b) \triangleq (|v|^2 + b) - y \log(|v|^2 + b). \quad (4)$$

In this expression we treat  $0 \log 0$  as being 0 because a Poisson random variable with zero mean can only take the value 0. One can verify that  $\psi$  has a well-defined ascent direction (negative of descent direction [17]):

$$\psi(v; y, b) = 2v \left( 1 - \frac{y}{|v|^2 + b} \right), \quad v \in \mathbb{C}. \quad (5)$$

Similar problems for the case  $b_i = 0$  have been considered previously [18–21]. Many optical sensors also have Gaussian readout noise [22, 23], so a more precise model would consider a sum of Gaussian and Poisson noise. However, the log likelihood for a Poisson plus Gaussian distribution is complicated, so a common approximation is to use a shifted Poisson model [24] that also leads to the cost function in (4).

One can verify that the function

$$h(r; y, b) \triangleq (r^2 + b) - y \log(r^2 + b), \quad r \in \mathbb{R}, \quad (6)$$

is nonconvex when  $0 < b < y$ . That property, combined with the modulus within the logarithm in (4), makes (4) a challenging optimization problem.

In most real-world applications, background counts are unlikely to be zero (e.g., considering naturally occurring background radiation). When  $b_i > 0$ , one can derive the following upper bound for the magnitude of the second-order ascent direction of  $\psi$ :

$$\begin{aligned} \ddot{\psi}(v; y, b) &= \text{sign}(v) \left( 2 + 2y \frac{|v|^2 - b}{(|v|^2 + b)^2} \right), \\ |\ddot{\psi}(v; y, b)| &\leq 2 + \frac{y}{4b}. \end{aligned} \quad (7)$$

This bounded curvature property enables us to construct a quadratic majorizer for (4) and derive an MM algorithm [25].

To handle the case when  $b_i = 0$ , where the curvature is unbounded, Section III-C develops an alternating direction method of multipliers (ADMM) with variable splitting  $v_i = \mathbf{a}'_i \mathbf{x}$ . One potential advantage of MM and ADMM algorithms over WF and GS is they can accommodate non-smooth regularizers, like the  $\ell_1$  norm, for which WF and GS are inapplicable [26]. Furthermore, if the regularizer is prox-friendly, then proximal gradient methods such as ISTA [27], FISTA [28] and POGM [29] can be applied in the inner minimization steps of both MM and ADMM algorithms.

The rest of this paper is organized as follows. Section II gives a brief overview of classical algorithms like WF and GS for phase retrieval. Section III introduces algorithms for Poisson phase retrieval, namely a modified Wirtinger flow method, and MM and ADMM algorithms. Section IV provides numerical results using simulated data under different experimental settings.

*Notation:* Bold upper/lower case letters (e.g.,  $\mathbf{A}$ ,  $\mathbf{x}$ ) denote matrices and column vectors, respectively. Italics (e.g.,  $\mu$ ,  $y$ ,  $b$ ) denote scalars.  $\mathbb{R}^N$  and  $\mathbb{C}^N$  denote  $N$ -dimensional real/complex normed vector space, respectively.  $(\cdot)^*$  denotes the complex conjugate and  $(\cdot)'$  denotes Hermitian transpose.  $\text{diag}\{\cdot\}$  is a diagonal matrix constructed from a column vector. Unless otherwise defined, a subscript denotes outer iterations and superscript denotes the inner iterations, respectively. For gradients associated with complex numbers/vectors, the notation  $\dot{\psi}(\cdot)$  and  $\nabla(\cdot)$ , should be considered as an ascent direction, not as a derivative.

## II. RELATED WORKS

The Wirtinger flow algorithm for gradient descent of the Gaussian cost function (2) uses the gradient [8]:

$$\nabla g(\mathbf{x}) = 4\mathbf{A}' \text{diag}\{|\mathbf{A}\mathbf{x}|^2 - \mathbf{y} + \mathbf{b}\} \mathbf{A}\mathbf{x}. \quad (8)$$

As discussed in [8], one issue associated with the Wirtinger flow algorithm is that it can be difficult to find a good scheduling term  $\mu$  partially because of the non-convexity of the cost function. Thus, the author of [8] uses a heuristic where  $\mu$  is rather small at the first few iterations and gradually becomes larger as the iterations count increases. A drawback of that approach is the need to select hyper-parameters that control the growing speed of  $\mu$ . An alternative approach is to perform a line search for  $\mu$  in each iteration [7], reducing  $\mu$  until the cost function decreases sufficiently. However, this approach can dramatically increase the compute time of the algorithm due to the variable number of inner iterations.

An alternative is to use the magnitude model rather than the intensity model (2), and introduce a new variable  $\boldsymbol{\theta}$  to represent the phase, which leads to the following optimization problem:

$$\begin{aligned} \hat{\mathbf{x}}, \hat{\boldsymbol{\theta}} &= \underset{\mathbf{x}, \boldsymbol{\theta} \in \mathbb{C}^N}{\text{argmin}} \|\mathbf{A}\mathbf{x} - \text{diag}\{\sqrt{\max(\mathbf{y} - \mathbf{b}, \mathbf{0})}\} \boldsymbol{\theta}\|_2^2, \\ \text{subject to } &|\theta_i| = 1, \quad i = 1, \dots, N. \end{aligned} \quad (9)$$

One can verify this cost function is also non-convex. To solve (9), one classical approach is the GS algorithm [9] that alternatively updates  $\mathbf{x}$  and  $\boldsymbol{\theta}$  in each iteration. WF and GS are two classic methods for phase retrieval under the Gaussian noise model.

## III. METHODS FOR POISSON MODEL

### A. Wirtinger Flow for Poisson model

To generalize the Wirtinger flow algorithm to the Poisson cost function (4), we simply replace the gradient (8) by (5) in its optimization framework.

Instead of doing a line search to find  $\mu$  as in [7], we propose to make a quadratic approximation along the gradient direction of the cost function at each iteration, and then apply one step of Newton's method to minimize that 1D quadratic. Because computing the Hessian can be computationally expensive in large-scale problems, we replace the Hessian by the observed Fisher information when applying Newton's method [30].

Specifically, letting  $\mathbf{x}_k$  denote the estimate of  $\mathbf{x}$  at the  $k$ th iteration, we first approximate the 1D line search problem associated with (4) by the following Taylor

series

$$\begin{aligned} \mu_k &= \underset{\mu \in \mathbb{R}}{\operatorname{argmin}} f_k(\mu), \\ f_k(\mu) &\triangleq f(\mathbf{x}_k + \mu \nabla f(\mathbf{x}_k)) \approx f(\mathbf{x}_k) + \|\nabla f(\mathbf{x}_k)\|_2^2 \mu \\ &\quad + \frac{1}{2} \nabla f(\mathbf{x}_k)' \nabla^2 f(\mathbf{x}_k) \nabla f(\mathbf{x}_k) \mu^2, \end{aligned} \quad (10)$$

where one can verify that the minimizer is

$$\mu_k = -\frac{\|\nabla f(\mathbf{x}_k)\|_2^2}{\nabla f(\mathbf{x}_k)' \nabla^2 f(\mathbf{x}_k) \nabla f(\mathbf{x}_k)}. \quad (11)$$

We next approximate the Hessian matrix  $\nabla^2 f(\mathbf{x})$  using the Fisher information matrix associated with ML estimation:

$$\begin{aligned} \nabla^2 f(\mathbf{x}) &\approx \mathbf{I}(\mathbf{x}, \mathbf{b}) \\ &\triangleq \mathbb{E}_{\mathbf{y}} \left[ (\nabla f(\mathbf{y}; \mathbf{x}, \mathbf{b})) (\nabla f(\mathbf{y}; \mathbf{x}, \mathbf{b}))' \middle| \mathbf{x}, \mathbf{b} \right] \\ &= \mathbf{A}' \mathbb{E}_{\mathbf{y}} \left[ (\dot{\psi}(\mathbf{y}; \mathbf{v}, \mathbf{b})) (\dot{\psi}(\mathbf{y}; \mathbf{v}, \mathbf{b}))' \middle| \mathbf{v}, \mathbf{b} \right] \mathbf{A}, \end{aligned} \quad (12)$$

where  $\dot{\psi}(\cdot)$  denotes element-wise application of the function  $\psi$  to its first argument (as in the Julia language). One can verify that the marginal Fisher information for a single term  $\dot{\psi}(\mathbf{y}; \mathbf{v}, \mathbf{b})$  is

$$\begin{aligned} I(v, b) &= \mathbb{E}_{\mathbf{y}} \left[ |\dot{\psi}(\mathbf{y}; \mathbf{v}, \mathbf{b})|^2 \middle| \mathbf{v}, \mathbf{b} \right] \\ &= \frac{4|v|^2}{|v|^2 + b}, \quad v \in \mathbb{C}, b > 0. \end{aligned} \quad (13)$$

Substituting (13) into (12) and substituting (12) into (11) yields the simplified expression

$$\mu_k \triangleq -\frac{\|\nabla f(\mathbf{x}_k)\|_2^2}{\mathbf{d}'_k \operatorname{diag}\{\mathbf{I}(\mathbf{A}\mathbf{x}_k, \mathbf{b})\} \mathbf{d}_k}, \quad (14)$$

where  $\mathbf{d}_k \triangleq \mathbf{A} \nabla f(\mathbf{x}_k)$ .

Similarly, the marginal Fisher information for the scalar case of the Gaussian cost function (2) is

$$I(v, b) = 16|v|^2(|v|^2 + b), \quad v \in \mathbb{C}, b \geq 0. \quad (15)$$

Substituting (15) into (14), one can also derive a convenient step size  $\mu_k$  for the WF algorithm for the Gaussian model (2) using its Fisher information to approximate the exact Hessian. This approach removes all tuning parameters other than number of iterations. Section IV used this approach to accelerate both the Gaussian and Poisson WF methods.

Algorithm 1 shows our modified Wirtinger flow (WF-Poisson) method using Fisher information to compute the step size.

---

**Algorithm 1:** Wirtinger flow for the Poisson model using Fisher information for step size

---

**Input:**  $\mathbf{A}, \mathbf{y}, \mathbf{b}$  and  $n$  (number of iterations)

Initialize:  $\mathbf{x}_0 \leftarrow$  random Gaussian vector

**for**  $k = 0, \dots, n - 1$  **do**

$$\begin{aligned} &\nabla f(\mathbf{x}_k) = \mathbf{A}' \dot{\psi}(\mathbf{A}\mathbf{x}_k; \mathbf{y}, \mathbf{b}) \\ &I(v, b) = 4|v|^2/(|v|^2 + b) \\ &\mathbf{d}_k = \mathbf{A} \nabla f(\mathbf{x}_k) \\ &\mu_k = -\|\nabla f(\mathbf{x}_k)\|_2^2 / (\mathbf{d}'_k \operatorname{diag}\{\mathbf{I}(\mathbf{A}\mathbf{x}_k, \mathbf{b})\} \mathbf{d}_k) \\ &\mathbf{x}_{k+1} = \mathbf{x}_k - \mu_k \nabla f(\mathbf{x}_k) \end{aligned}$$

**end**

**Output:**  $\mathbf{x}_n$

---

### B. An MM approach with a quadratic majorizer

A majorize-minimize (MM) algorithm [31], as a generalization of the expectation-maximization (EM) algorithm, solves an optimization problem by iteratively constructing and solving simpler surrogate optimization problems. Quadratic majorizers are very common in MM algorithms because they have closed-form solutions and are well-suited to conjugate gradient methods.

When  $b_i = 0$ , one can verify  $\dot{\psi}$  has a singularity at  $v = 0$ , which means  $\psi$  is not Lipschitz differentiable, so we need to pursue other algorithms for this case, as discussed in a subsequent section. In contrast, if  $b_i > 0$ , one can construct a quadratic majorizer on  $\mathbb{R}$  for (6), as illustrated in Fig. 1. With a bit more work to generalize to  $\mathbb{C}^N$ , a quadratic majorizer for the Poisson ML cost function (4) can be constructed as

$$\begin{aligned} q(\mathbf{x}; \mathbf{x}_k) &\triangleq f(\mathbf{x}_k) + \operatorname{real}\left\{ (\mathbf{x} - \mathbf{x}_k)' \mathbf{A}' \dot{\psi}(\mathbf{A}\mathbf{x}_k; \mathbf{y}, \mathbf{b}) \right\} \\ &\quad + \frac{1}{2} (\mathbf{x} - \mathbf{x}_k)' \mathbf{A}' \mathbf{W} \mathbf{A} (\mathbf{x} - \mathbf{x}_k), \end{aligned} \quad (16)$$

where  $\mathbf{W}$  denotes a diagonal curvature matrix. From (7), one choice of  $\mathbf{W}$  uses the maximum of  $\dot{\psi}$ :

$$\mathbf{W}_{\max} \triangleq \operatorname{diag}\{2 + \mathbf{y}/(4\mathbf{b})\} \in \mathbb{R}^{M \times M}. \quad (17)$$

However, this curvature matrix is suboptimal because the curvature of quadratic majorizers of  $\psi(v; \cdot)$  varies with  $v = [\mathbf{A}\mathbf{x}_k]_i$ . For example, when  $|v| \rightarrow \infty$ , then (4) is dominated by the quadratic term having curvature 2 so that if  $y$  is large and  $b$  is small, then the majorizing curvature can be much greater than the optimal curvature 2. Thus, instead of using  $\mathbf{W}_{\max}$ , we propose to use the following improved curvature:

$$\begin{aligned} \mathbf{W}_{\text{imp}} &\triangleq \operatorname{diag}\{c(\mathbf{A}\mathbf{x}_k; \mathbf{y}, \mathbf{b})\} \in \mathbb{R}^{M \times M}, \\ c(s; y, b) &\triangleq \begin{cases} \dot{\psi}\left(\frac{b + \sqrt{b^2 + b|s|^2}}{|s|}; y, b\right), & s \neq 0, \\ 2, & s = 0. \end{cases} \end{aligned} \quad (18)$$

One can verify  $\lim_{s \rightarrow 0} c(s; y, b) = 2$  so (18) is continuous over  $s \in \mathbb{C}$ . Appendix A proves that (18) provides a majorizer in (16) and is an improved curvature, though it is not necessarily the sharpest possible [32].

For the ML case where constraints or regularizers are absent, the quadratic majorizer (16) associated with (17) or (18) leads to the following MM update:

$$\begin{aligned} \mathbf{x}_{k+1} &= \underset{\mathbf{x} \in \mathbb{C}^N}{\operatorname{argmin}} q(\mathbf{x}; \mathbf{x}_k) \\ &= \mathbf{x}_k - (\mathbf{A}'\mathbf{W}\mathbf{A})^{-1} \mathbf{A}'\dot{\psi}(\mathbf{A}\mathbf{x}_k; \mathbf{y}, \mathbf{b}), \end{aligned} \quad (19)$$

When  $N$  is large the matrix inverse operation in (19) is impractical, so one alternative way is to run a few inner iterations of conjugate gradient (CG) to descend the quadratic majorizer and hence descend the original cost function.

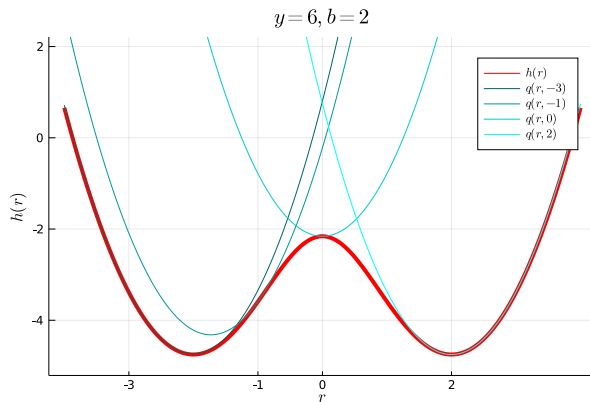


Fig. 1: Quadratic majorizers for the nonconvex Poisson log-likelihood function  $h(r; y, b)$  when  $y = 6$  and  $b = 2$ .

When one includes regularizers in the cost function (4), one can use the quadratic majorizer as the foundation for a proximal method if the regularizer is prox-friendly. The gradient of the majorizer  $q(\mathbf{x}; \mathbf{x}_k)$  has (best) Lipschitz constant  $\mathcal{L} = \|\mathbf{A}'\mathbf{W}\mathbf{A}\|_2$  that can be precomputed when  $\mathbf{W} = \mathbf{W}_{\max}$ , e.g., by the power method. When  $\mathbf{W} = \mathbf{W}_{\text{imp}}$ , the Lipschitz constant changes each iteration, so instead we used the inequality  $\|\mathbf{A}'\mathbf{W}\mathbf{A}\|_2 \leq \|\mathbf{A}'\mathbf{A}\|_2 \|\mathbf{W}\|_2$ , and seek for an upper bound for  $\|\mathbf{A}'\mathbf{A}\|_2$ .

Here we choose the regularizer as  $\beta\|\mathbf{T}\mathbf{x}\|_1$ , where  $\mathbf{T} \in \mathbb{C}^{K \times N}$  is a transform matrix. This is a common regularizer in signal processing and computational imaging that assumes the coefficients of a transformation of the true signal/image are approximately sparse. Based on (16), the minimization step of a MM algorithm for the regularized optimization problem is

$$\mathbf{x}_{k+1} = \underset{\mathbf{x} \in \mathbb{C}^N}{\operatorname{argmin}} q(\mathbf{x}; \mathbf{x}_k) + \beta\|\mathbf{T}\mathbf{x}\|_1. \quad (20)$$

If  $\mathbf{T}$  is prox-friendly, e.g., an orthogonal discrete wavelet transform (ODWT) matrix, then one can apply proximal gradient methods [27–29] to solve (20). For example, an iterative soft-thresholding algorithm (ISTA) algorithm is

$$\begin{aligned} \tilde{\mathbf{x}}_k^{(i)} &= \mathbf{x}_k^{(i)} - \frac{1}{\mathcal{L}} \nabla q(\mathbf{x}_k^{(i)}; \mathbf{x}_k), \\ \mathbf{x}_k^{(i+1)} &= \mathbf{T}' \operatorname{soft}(\mathbf{T} \tilde{\mathbf{x}}_k^{(i)}, \beta/\mathcal{L}), \\ \nabla q(\mathbf{x}; \mathbf{x}_k) &\triangleq \mathbf{A}'\mathbf{W}\mathbf{A}(\mathbf{x} - \mathbf{x}_k) + \mathbf{A}'\dot{\psi}(\mathbf{A}\mathbf{x}_k; \mathbf{y}, \mathbf{b}), \end{aligned} \quad (21)$$

where  $\mathbf{x}_k^{(0)} \triangleq \mathbf{x}_k$  denotes the initial estimate and the superscript  $i$  denotes the  $i$ th inner ISTA iteration in the  $k$ th outer MM iteration. For faster convergence rate, we used POGM [29] instead of ISTA in our simulations (Section IV).

If  $\mathbf{T}$  is not prox-friendly, e.g., the finite difference matrix used in total variation (TV) regularization, then we can replace (20) by a two-block cost function:

$$\begin{aligned} \mathbf{x}_{k+1}, \mathbf{z}_{k+1} &= \underset{\mathbf{x} \in \mathbb{C}^N, \mathbf{z} \in \mathbb{C}^K}{\operatorname{argmin}} Q_k(\mathbf{x}, \mathbf{z}), \\ Q_k(\mathbf{x}, \mathbf{z}) &\triangleq q(\mathbf{x}; \mathbf{x}_k) + \beta \left( \frac{1}{2} \|\mathbf{T}\mathbf{x} - \mathbf{z}\|_2^2 + \alpha \|\mathbf{z}\|_1 \right), \end{aligned} \quad (22)$$

where one can alternatively update  $\mathbf{x}$  and  $\mathbf{z}$ . The  $\mathbf{x}$  update uses the closed-form solution that involves matrix inverse or conjugate gradient. The  $\mathbf{z}$  update is simply a soft-thresholding operation.

### C. ADMM

As mentioned in the previous section, MM algorithms are inapplicable when  $b_i = 0$  because they require the curvature of  $\psi$  to be bounded. To handle the case when  $b_i = 0$ , we developed an ADMM algorithm with variable splitting  $v_i = \mathbf{a}'_i \mathbf{x}$ . This ADMM algorithm can be generalized to  $b_i > 0$  by a simple modification of the  $v_i$  update.

In particular, an augmented linearized Lagrangian of (4) when  $b_i = 0$  is given by

$$\begin{aligned} L_\rho(\mathbf{v}, \mathbf{x}; \boldsymbol{\eta}, \rho) &= \sum_i \left[ (|v_i|^2) - y_i \log(|v_i|^2) \right] \\ &\quad + \frac{\rho}{2} \sum_i \left[ |v_i - \mathbf{a}'_i \mathbf{x} + \eta_i|^2 - |\eta_i|^2 \right], \end{aligned} \quad (23)$$

where  $\boldsymbol{\eta}$  is the dual variable and  $\rho > 0$  denotes the AL penalty parameter.

We followed the order of first updating  $\mathbf{v}$ , then  $\mathbf{x}$  and finally  $\boldsymbol{\eta}$ . Note that the updates for the phase and magnitude of  $\mathbf{v}$  are separable, so we first update the phase of  $\mathbf{v}$  then update its magnitude. In particular, the

phase update is

$$\text{sign}(\mathbf{v}_{k+1}) = \text{sign}(\mathbf{A}\mathbf{x}_k - \boldsymbol{\eta}_k). \quad (24)$$

For the  $|\mathbf{v}|$  update, set  $t_i = |\mathbf{a}'_i \mathbf{x}_k - \eta_i|$ ; then the block update of  $|\mathbf{v}|$  has component  $|v_i|$  determined by the stationary condition:

$$0 = 2|v_i| - \frac{2y_i}{|v_i|} + \rho(|v_i| - t_i). \quad (25)$$

Equality (25) can be transformed into a quadratic with the following nonnegative solution:

$$|v_i| = \frac{\rho t_i + \sqrt{\rho^2 t_i^2 + 8y_i(2 + \rho)}}{2(2 + \rho)}. \quad (26)$$

In the unregularized case, the  $\mathbf{x}$  update is a simple least square (LS) problem:

$$\mathbf{x}_{k+1} = (\mathbf{A}'\mathbf{A})^{-1}\mathbf{A}'(\mathbf{v}_{k+1} + \boldsymbol{\eta}_k). \quad (27)$$

Similar to (19), if  $N$  is large, then we run a few iterations of CG to update  $\mathbf{x}$  in (27), instead of calculating  $(\mathbf{A}'\mathbf{A})^{-1}$ .

When we consider a non-smooth regularizer  $\|\mathbf{T}\mathbf{x}\|_1$ , the  $\mathbf{x}$  update becomes

$$\mathbf{x}_{k+1} = \underset{\mathbf{x} \in \mathbb{C}^N}{\text{argmin}} \frac{\rho}{2} \|\mathbf{A}\mathbf{x} - \mathbf{v}_{k+1} - \boldsymbol{\eta}_k\|_2^2 + \beta \|\mathbf{T}\mathbf{x}\|_1. \quad (28)$$

Again, if  $\mathbf{T}$  is prox-friendly, methods such as ISTA, FISTA and POGM can also be applied here. If not, we expand (28) into

$$\begin{aligned} \mathbf{x}_{k+1}, \mathbf{z}_{k+1} = \underset{\mathbf{x} \in \mathbb{C}^N, \mathbf{z} \in \mathbb{C}^K}{\text{argmin}} & \frac{\rho}{2} \|\mathbf{A}\mathbf{x} - \mathbf{v}_{k+1} - \boldsymbol{\eta}_k\|_2^2 \\ & + \beta \left( \frac{1}{2} \|\mathbf{T}\mathbf{x} - \mathbf{z}\|_2^2 + \alpha \|\mathbf{z}\|_1 \right), \end{aligned} \quad (29)$$

and alternatively update  $\mathbf{x}$  and  $\mathbf{z}$ .

The dual variable  $\boldsymbol{\eta}$  ascent update is simply [33]:

$$\boldsymbol{\eta}_{k+1} = \boldsymbol{\eta}_k + (\mathbf{v}_{k+1} - \mathbf{A}\mathbf{x}_{k+1}). \quad (30)$$

For the case  $b_i > 0$ , everything is the same as the case  $b_i = 0$  except the update for  $|v_i|$ , for which one can verify the stationarity condition becomes

$$0 = 2|v_i| - \frac{2y_i|v_i|}{|v_i|^2 + b_i} + \rho(|v_i| - t_i), \quad (31)$$

which reduces to the cubic

$$0 = (2 + \rho)|v_i|^3 - \rho t_i |v_i|^2 + (2b_i - 2y_i + \rho b_i)|v_i| - \rho b_i t_i. \quad (32)$$

Owing to the intermediate value theorem and the non-negativity of  $\rho$ ,  $b_i$ ,  $t_i$ , this cubic (32) can only possess

one or three positive real roots. If the cubic has one positive root, then the update of  $|v_i|$  is simply to assign the single positive root. If the cubic has three positive roots, we choose the root that minimizes the following Lagrangian term based on (33):

$$(|v_i|^2 + b_i) - y_i \log(|v_i|^2 + b_i) + \frac{\rho}{2} (|v_i| - t_i)^2. \quad (33)$$

A natural extension is to vary AL penalty parameter along with the variable update every few iterations. Boyd [33] *et al.*, considered the magnitude of primal residual  $\mathbf{r}_{k+1} = \mathbf{A}\mathbf{x}_{k+1} - \mathbf{v}_{k+1}$  and dual residual  $\mathbf{s}_{k+1} = \rho\mathbf{A}'(\mathbf{v}_{k+1} - \mathbf{v}_k)$ , as a principle to select penalty parameter to potentially improve convergence for convex optimization problems. However, for non-convex problems, the penalty parameter  $\rho$  is preferred to be sufficiently large to enable the convergence of ADMM algorithm [34]. Thus, we use of the following heuristic to update  $\rho$ :

$$\rho_{k+1} = \begin{cases} 2\rho_k, & \|r_k\| > 10\|s_k\| \\ \rho_k/2, & \|s_k\| > 100\rho_k\|r_k\| \\ \rho_k, & \text{otherwise.} \end{cases} \quad (34)$$

#### IV. NUMERICAL SIMULATIONS

This section reports numerical simulations that compare the convergence rates of the various algorithms and demonstrate that using the Poisson log likelihood improves the quality of the estimates under various experimental settings.

##### A. Experiment setup

We investigated 3 choices for the system matrix  $\mathbf{A}$ : complex random Gaussian matrix, DFT matrix, and an empirical transmission matrix. We ran all algorithms for 500 iterations on a server with Ubuntu 16.04 LTS operating system having Intel(R) Xeon(R) CPU E5-2698 v4 @ 2.20GHz and 251 GB memory. We found that running few iterations of CG gave almost the same reconstructed quality as performing matrix inverse but was somewhat (or much) faster (see supplemental figures S.2) when solving least square problems (19), (22), (27), (29). So we used the CG algorithm whenever possible in the algorithms mentioned in section III. In particular, we ran 3 iterations of CG in the first 10 outer iterations (out of 500 iterations) and only 1 CG update (equivalent to steepest gradient descent) after that.

The algorithms compared in this section are abbreviated as follows.

- WF-Gaussian and WF-Poisson: Wirtinger Flow algorithms based on the Gaussian/Poisson model, using Fisher information to select the step size
- GS: the Gerchberg Saxton algorithm based on the Gaussian model (9).
- LSMM: Unregularized MM algorithm with quadratic majorizer using the improved curvature.
- ADMM: Unregularized ADMM algorithm with adaptive AL penalty parameter ( $\rho$ ) that is initialized as 16.
- Regularized MM and ADMM: These algorithms use the regularizer  $\beta\|T\mathbf{x}\|_1$ , where  $T$  denotes the finite difference matrix or ODWT matrix. The regularized ADMM uses the same AL penalty parameter strategy as the unregularized ADMM.

All elements in the measurement vector  $\mathbf{y}$  were simulated to follow independent Poisson distributions per (3). To handle the phase ambiguity (all the algorithms can recover the signal only to within a constant phase shift due to the loss of global phase information), we used the following normalized root mean square error (NRMSE) metric [7] to evaluate all the algorithms:

$$\text{NRMSE} = \frac{\|\hat{\mathbf{x}} - \mathbf{x}_{\text{true}} e^{i\phi}\|_2}{\|\mathbf{x}_{\text{true}}\|_2}, \quad e^{i\phi} = \text{sign}(\mathbf{x}'_{\text{true}}\hat{\mathbf{x}}), \quad (35)$$

where  $\hat{\mathbf{x}}$  and  $\mathbf{x}_{\text{true}}$  denote the reconstructed signal/image and the true signal/image, respectively.

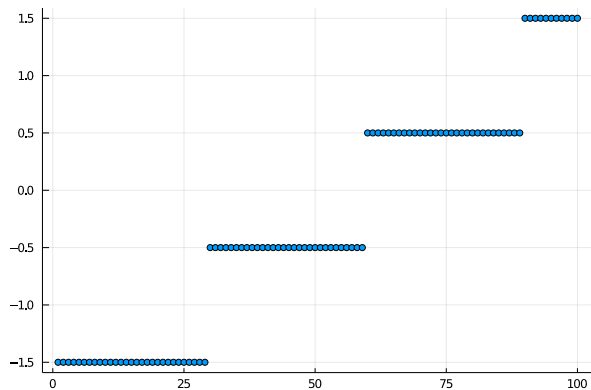
### B. Random Gaussian sensing matrix

First we consider the case when all the elements in the system matrix  $\mathbf{A}$  are independent random variables following a complex Gaussian distribution. We scaled  $\mathbf{A}$  by a constant such that the average of  $|\mathbf{a}'_i \mathbf{x}_{\text{true}}|^2$  is 2. The mean background counts ( $b$ ) were set to 0.1.

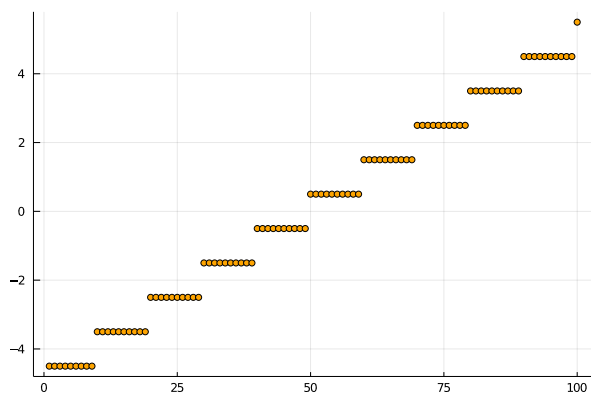
We adopted two finite length ( $N = 100$ ) signals as the true signal. The first finite length signal is a real, piece-wise constant signal ( $\mathbf{x}_{\text{true-A}}$ ); the second is a complex signal ( $\mathbf{x}_{\text{true-B}}$ ) whose real part is the same as  $\mathbf{x}_{\text{true-A}}$  and with a piece-wise constant imaginary part. Fig. 2 shows the real signal  $\mathbf{x}_{\text{true-A}}$  and the imaginary part of  $\mathbf{x}_{\text{true-B}}$ .

Here we exploit the piece-wise uniformity of the true signal, for which a natural choice for  $T$  is finite differences, i.e., a discrete TV regularizer. We denote the LSMM and ADMM algorithms using the TV regularizer as LSMM-TV and ADMM-TV, respectively. We chose the number of measurements  $M$  to range from 2000 to 6000. We repeated each experiment 10 times and averaged the results to reduce the effects of statistical randomness. We chose empirically the regularizer parameters  $\beta = 32$

and  $\alpha = 32$  in (22) and (29). We used 3 iterations of CG to update  $\mathbf{x}$  in (22) and (29).



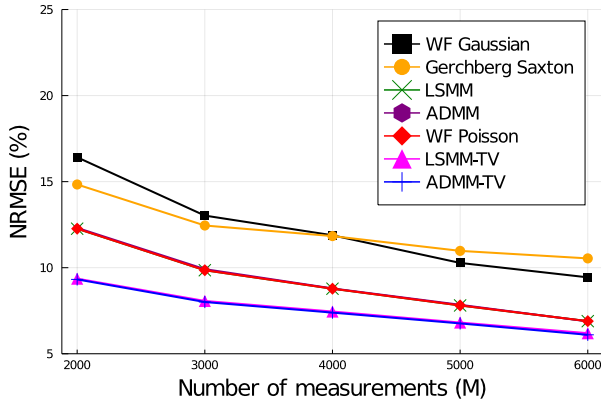
(a) real, piece-wise constant signal  $\mathbf{x}_{\text{true-A}}$ .



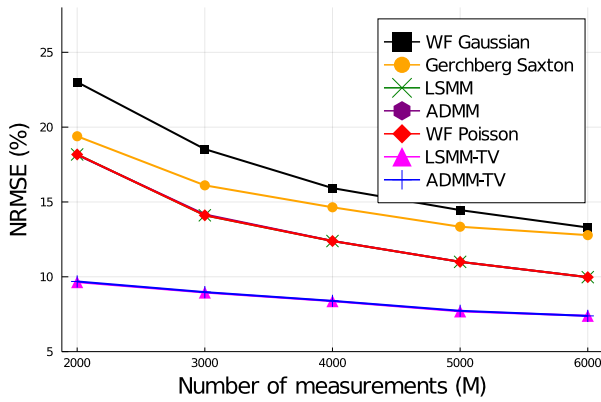
(b) The imaginary part of the complex signal  $\mathbf{x}_{\text{true-B}}$ .

Fig. 2: True signals used in simulations when  $\mathbf{A}$  is random Gaussian.

1) *Accuracy comparison:* Fig. 3 and Fig. 4 compare the NRMSE of all algorithms for  $b_i > 0$  and  $b_i = 0$ , respectively. As expected, algorithms based on the Poisson model produce consistently better quality results (lower NRMSE) than algorithms based on the Gaussian model. Furthermore, improvements are more notable for  $b_i = 0$  than  $b_i > 0$ , possibly because  $\mathbb{E}[\mathbf{y}]$  is even lower when  $b_i = 0$  than  $b_i > 0$ , so the Gaussian model may perform even worse in that case. In Fig. 3, WF-Poisson, LSMM and ADMM all overlap, perhaps because they all reached a global minimizer. In addition, the regularized algorithms (LSMM-TV and ADMM-TV) led to the lowest NRMSE and were less sensitive to the change of  $M$  than the unregularized algorithms. The regularizers exploit assumed properties of the true signal that can help the algorithms estimate  $\mathbf{x}$  when the measurements are noisy or corrupted. In our experiment, the photon's arrival-rate is low so that  $\mathbf{y}$  is very noisy, thus regularizers can significantly improve the reconstruction quality.



(a)

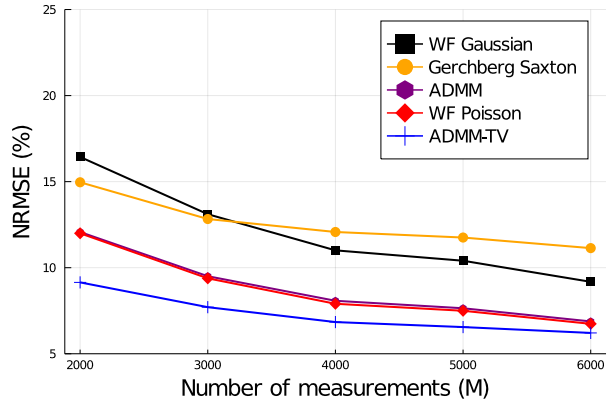


(b)

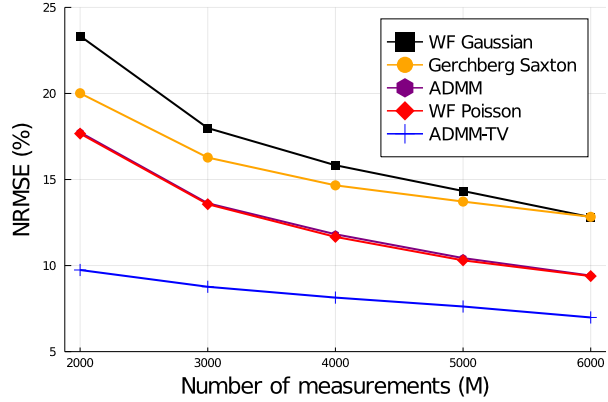
Fig. 3: NRMSE vs. number of measurements ( $M$ ) when  $\mathbf{A}$  is random Gaussian and  $b_i > 0$ , where (a) and (b) correspond to  $\mathbf{x}_{\text{true-A}}$  (real) and  $\mathbf{x}_{\text{true-B}}$  (complex), respectively.

ADMM and WF Poisson do not perfectly overlap in Fig. 4, perhaps because  $\rho$  is not sufficiently large to enable the ADMM algorithm to converge to a global minimizer. In particular, when  $b_i = 0$ , the logarithm in (23) is unbounded if  $|v_i| \rightarrow 0$  so a larger  $\rho$  might be needed to compensate. However, a large  $\rho$  could slow convergence speed (results not shown), so there may be a trade-off between convergence to global minimizers and the convergence speed. In addition, Fig. 3 and Fig. 4 both showed that when  $M = 2000$ , the regularized algorithms improve NRMSE the most compared to unregularized algorithms. This also illustrates when the number of measurements is low, a regularizer can be very helpful in enhancing the quality of the recovered signals/images.

2) *Speed comparison:* Fig. 5 and Fig. 6 compare how quickly different algorithms decrease the NRMSE when the number of measurements is  $M = 3000$ . The regularized algorithms are slower because they involve inner-



(a)



(b)

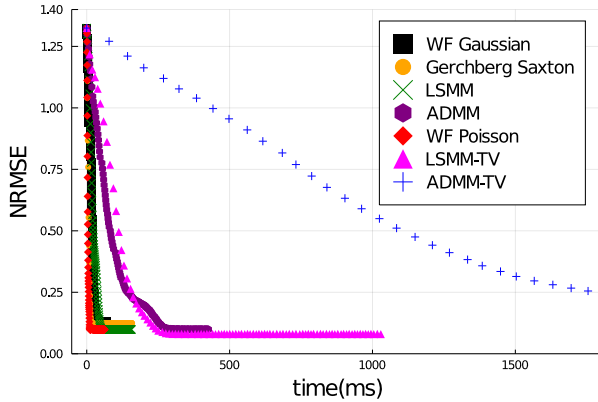
Fig. 4: NRMSE vs. number of measurements ( $M$ ) when  $\mathbf{A}$  is random Gaussian and  $b_i = 0$ , where (a) and (b) correspond to  $\mathbf{x}_{\text{true-A}}$  and  $\mathbf{x}_{\text{true-B}}$ , respectively.

iterations. Interestingly, WF Poisson decreases NRMSE faster than WF Gaussian, especially when  $\mathbf{x}_{\text{true}}$  is complex. Our reasons for this are as follows. Firstly, the Poisson model is more suitable than the Gaussian model in our experiment where  $\mathbf{y}$  has a Poisson distribution. Secondly, the quadratic approximation fits better to (4) than (2) because (4) is more similar to a quadratic function, i.e., has bounded curvature when  $b_i > 0$ , whereas (2) is a quartic with unbounded curvature.

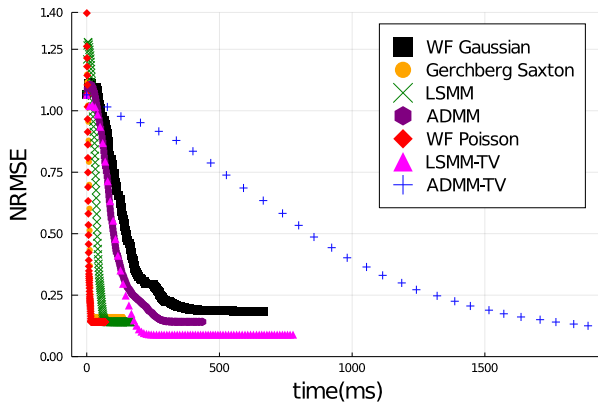
### C. Discrete Fourier transform matrix

Next we consider the case where the system matrix  $\mathbf{A}$  is a DFT matrix. As discussed in [35], in the classical Fourier phase retrieval problem, the measurement vector  $\mathbf{y}$  is given by

$$y[\tilde{n}] = \left| \sum_{n=0}^{N-1} x[n] e^{-i2\pi n\tilde{n}/N} \right|^2 + b[\tilde{n}], \quad \tilde{n} = 0, \dots, \tilde{N}-1, \quad (36)$$



(a)



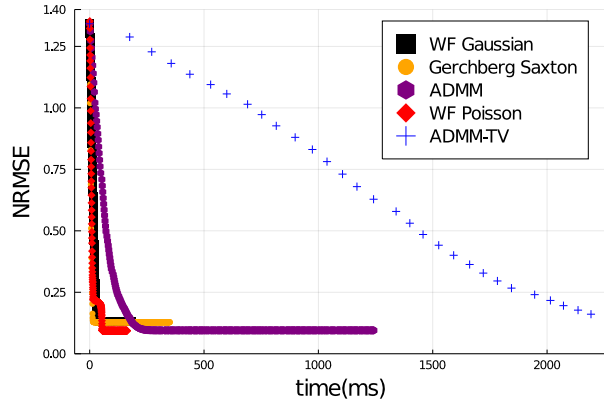
(b)

Fig. 5: NRMSE vs. time (ms) when  $\mathbf{A}$  is random Gaussian,  $M = 3000$  and  $b_i > 0$ . Subfigure (a) and (b) correspond to  $\mathbf{x}_{\text{true-A}}$  and  $\mathbf{x}_{\text{true-B}}$ , respectively.

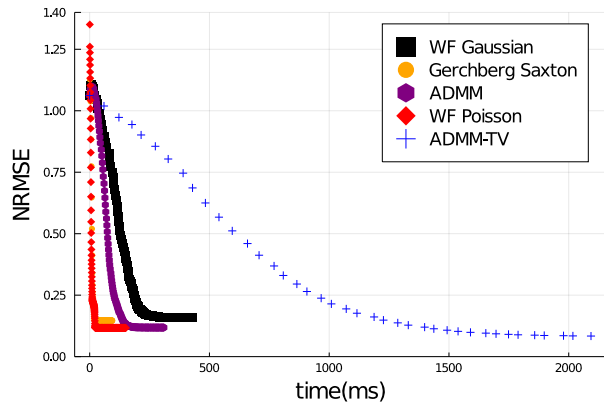
where  $\tilde{N} = 2N - 1$  (here we consider the over-sample case [35]). Compared to when  $\mathbf{A}$  is random Gaussian, where the only ambiguity is the global constant phase shift, the Fourier case involves more ambiguities such as circular shift and conjugate inversion [36]. To circumvent these ambiguities, one method is to use several different masks that introduce redundancy in the measurement vector  $\mathbf{y}$ . Specifically, the measurement model becomes:

$$y_l[\tilde{n}] = \left| \sum_{n=0}^{N-1} x[n] D_l[n] e^{-i2\pi n\tilde{n}/\tilde{N}} \right|^2 + b_l[\tilde{n}], \quad (37)$$

where  $\mathbf{y}_l \in \mathbb{R}^{\tilde{N}}$  for  $l = 1, \dots, L$  and  $D_l$  denotes the  $l$ th of  $L$  masks. Here  $M = L\tilde{N}$ . Our experiment used  $L = 21$  masks to define the overall system matrix  $\mathbf{A}$ , where the first mask has full sampling and the remaining 20 have sampling rate 0.5 with randomly sampling pattern. We scaled the system matrix  $\mathbf{A}$  by a constant  $c_{\text{diff}}$  so that the average of  $|\mathbf{a}'_i \mathbf{x}_{\text{true}}|^2$  is 1 and the background counts vector  $\mathbf{b}$  was set to 0.1.



(a)



(b)

Fig. 6: NRMSE vs. time (ms) when  $\mathbf{A}$  is random Gaussian,  $M = 3000$  and  $b_i = 0$ . Subfigure (a) and (b) correspond to  $\mathbf{x}_{\text{true-A}}$  and  $\mathbf{x}_{\text{true-B}}$ , respectively.

Our true image is the Shepp-Logan phantom of size  $256 \times 256$  with pixel values ranging from 0 to 9. Here we exploit the fact that the detail coefficients of the discrete wavelet transform of the true image are sparse, so we chose the matrix  $\mathbf{T}$  in the regularizer to be an ODWT matrix. Because the pixel values in an image cannot be negative, we initialize  $\mathbf{x}$  as a random vector following a uniform distribution on  $[0, 1]$ . We chose empirically the regularization parameter  $\beta = 4$  in (20) and (28). We ran 10 inner iterations of POGM with adaptive restart [29] for each outer iteration.

When  $\mathbf{A}$  is a DFT matrix, the dynamic range of the  $y_i$  values can be very wide, leading to an ill-conditioned curvature matrix  $\mathbf{W}$ . In particular, the curvature changes dramatically across different coordinates, and the MM algorithm based on a quadratic majorizer using the maximum or improved curvature can converge very slowly (results not shown). Thus, for the DFT case we imposed a threshold on the elements of the curvature matrix  $\mathbf{W}$

as follows:  $\tilde{\mathbf{W}} = \min(\mathbf{W}, \mathbf{W}_\mu + 3 * \mathbf{W}_\sigma)$ , where  $\mathbf{W}_\mu$  and  $\mathbf{W}_\sigma$  denote the mean and the standard deviation of the diagonal elements of the original  $\mathbf{W}$ , respectively. We used  $\tilde{\mathbf{W}}$  to construct quadratic ‘‘majorizers’’ for the DFT case.

Fig. 7 compares the images reconstructed by the WF, GS, MM and ADMM algorithms. Similar to the results in [7] where the WF-Gaussian algorithm was shown to have very low recovery probability when  $\mathbf{A}$  is a DFT matrix, the WF-Gaussian algorithm in our experiment also failed to reconstruct the image. Again, algorithms based on the Poisson model had better reconstruction quality than algorithms derived from Gaussian model. It is computationally expensive to directly compute the best Lipschitz constant ( $\mathcal{L} = \|\mathbf{A}'\mathbf{W}\mathbf{A}\|_2$ ) every time  $\mathbf{W}$  changes, so we used  $\mathcal{L} = c_{\text{dft}}^2 \tilde{N}^2 L \|\tilde{\mathbf{W}}\|_2$  in MM algorithms, where one can verify  $\|\mathbf{A}'\mathbf{A}\|_2 \leq c_{\text{dft}}^2 \tilde{N}^2 L$ , where  $c_{\text{dft}}$  is the scaling factor applied to  $\mathbf{A}$ .

#### D. Empirical transmission matrix

As discussed in [37, 38], a transmission matrix  $\mathbf{A}$  can be learned empirically through physical experiments. We chose the empirical transmission matrix (of size  $65536 \times 256$ ) that was learned using the prVAMP algorithm [38] and uniformly sampled 10000 rows of it so that  $\mathbf{A} \in \mathbb{C}^{10000 \times 256}$ . Unlike in the previous sections where we scaled the system matrix  $\mathbf{A}$ , here we keep  $\mathbf{A}$  fixed and scaled pixel values in the true image (Fig. 8) to have pixel range from 0 to 0.25. With this scaling, the average of  $|\mathbf{a}_i' \mathbf{x}_{\text{true}}|^2$  was 1.14. The true image was selected from the dataset provided in [38], where all images have pixel values ranging from 0 to 255 before scaling. The background counts  $\mathbf{b}$  were set to 0.1. Again, we chose  $\mathbf{T}$  to be an ODWT matrix to exploit sparsity of the true image’s discrete wavelet transform. We chose the regularization parameter to be  $\beta = 32$  in (20) and (28) and we ran 3 inner iterations of POGM for each outer iteration.

Fig. 8 shows the images reconstructed using different algorithms. The Poisson methods (WF Poisson, LSMM, ADMM) all demonstrated noticeably improved image quality and reduced NRMSE compared to Gaussian methods (WF Gaussian, GS). The regularized Poisson methods (LSMM-ODWT, ADMM-ODWT) further improved the image quality.

## V. CONCLUSION

This paper describes and compares several algorithms including Wirtinger flow (WF), Gerchberg Saxton

(GS), majorize-minimize (MM) and alternating direction method of multipliers (ADMM), for ML estimation and regularized ML estimation for phase retrieval from Poisson measurements. We also proposed several modifications to the WF and MM algorithms to potentially improve their computational efficiencies. For the WF algorithm, instead of doing a line search or using a heuristic step size, we used a quadratic approximation along the gradient direction and replaced the Hessian by the observed Fisher information so that the step size can be computed efficiently without any tuning parameter. For the MM algorithm with quadratic majorizers, we proposed a curvature formula and proved that it is superior to the curvature built on the upper bound of the second derivative of the Poisson ML cost function, i.e., the Lipschitz constant of its derivative.

Simulation results showed that the ML estimates based on the Poisson model (WF Poisson, MM, ADMM) yielded consistently lower NRMSE than algorithms based on Gaussian ML model (WF Gaussian and GS), when tested on real/complex simulated signals/images with different system matrices (random complex Gaussian, discrete Fourier transform (DFT) and an empirical transmission matrix), for measurements having Poisson noise when background counts  $b_i > 0$ . For  $b_i = 0$ , simulation results showed that Poisson methods (WF Poisson, ADMM) also produced consistently lower NRMSE than Gaussian methods (WF Gaussian, GS) with random complex Gaussian system matrix. Furthermore, as expected the regularized algorithms designed for the Poisson model that exploit assumed properties of the true signals/images, such as sparsity of finite differences (anisotropic total variation) or of the coefficients of a discrete wavelet transform, can further lower the NRMSE compared to unregularized algorithms. Regarding the computational efficiency, in the unregularized case, the WF Poisson algorithm and Gerchberg Saxton decreased the NRMSE fastest but WF Poisson demonstrated higher reconstruction quality. In the regularized case, the regularized LSMM algorithm decreased the NRMSE with comparable speed performance as the unregularized algorithms, but with notably improved reconstruction accuracy (lower NRMSE).

In summary, the proposed algorithms are effective for both regularized and unregularized phase retrieval from Poisson measurements. Future works include establishing sufficient conditions for global convergence, investigating algorithms that can handle other kind of regularizers (e.g.,  $\ell_0$  norm, deep learning methods), seeking the optimal or closer to optimal curvature, and testing algorithms derived for the Poisson noise model under a wider variety of experimental settings.

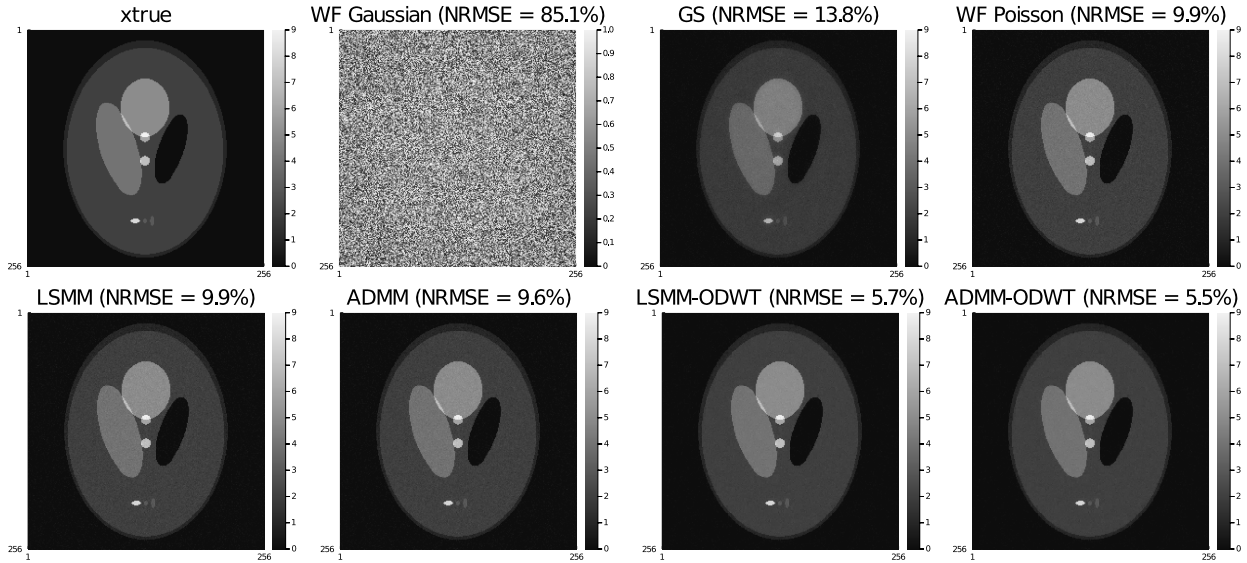


Fig. 7: Reconstructed image and corresponding NRMSE compared to the true image (Shepp-Logan phantom of size  $256 \times 256$ ), for a sensing system with  $L = 21$  masked DFT matrices. The average of  $|a_i^l x|^2$  and  $b_i$  were set to 1 and 0.1, respectively.

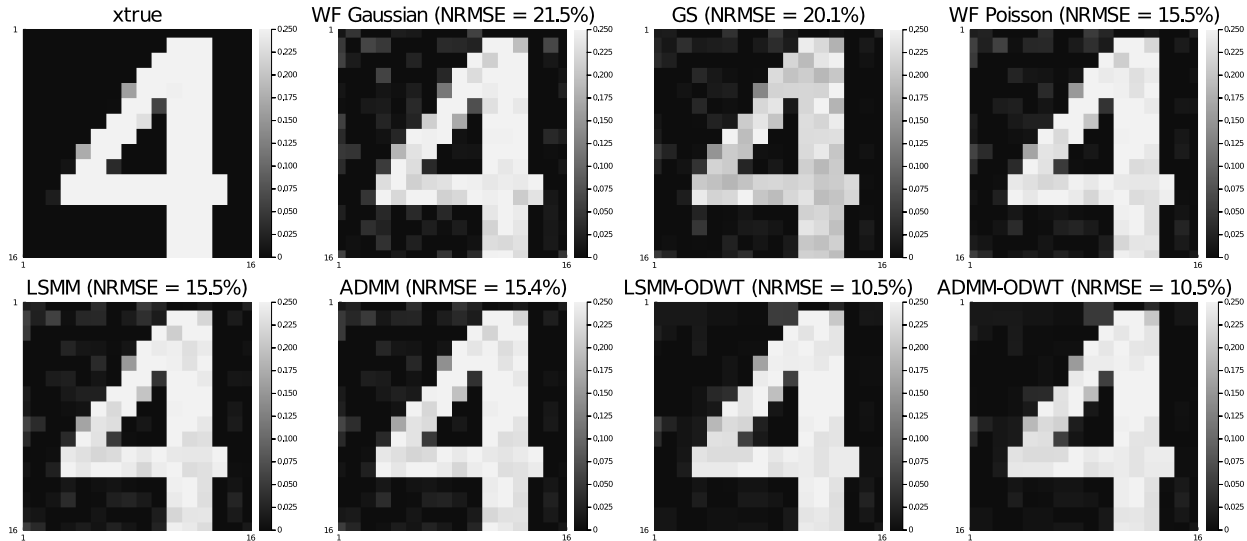


Fig. 8: Reconstructed images and their corresponding NRMSE compared to the true image (of size  $16 \times 16$ ), using an empirical system matrix from [38] with  $M = 10000$ .

## VI. REFERENCES

- [1] K. Jaganathan, Y. C. Eldar, and B. Hassibi. *Phase retrieval: an overview of recent developments*. 2015.
- [2] P. Grohs, S. Koppensteiner, and M. Rathmair. “Phase retrieval: uniqueness and stability”. In: *SIAM Review* 62.2 (2020), 301–50.
- [3] P. Jaming. “Phase retrieval techniques for radar ambiguity problems.” In: *J. Four. Anal. Appl.* 5.4 (1999), pp. 309–329.
- [4] R. P. Millane. “Phase retrieval in crystallography and optics”. In: *J. Opt. Soc. Am. A* 7.3 (Mar. 1990), 394–411.
- [5] J. Dainty and J. Fienup. “Phase retrieval and image reconstruction for astronomy”. In: *Imag. Recov. Theory Appl.* 13 (Jan. 1987), pp. 231–275.

- [6] L. R. Rabiner and B.-H. Juang. *Fundamentals of Speech Recognition*. Eng. Clif., NJ: Pren. Hall, 1993.
- [7] T. Qiu, P. Babu, and D. P. Palomar. “PRIME: phase retrieval via majorization-minimization”. In: *IEEE Trans. Sig. Proc.* 64.19 (Oct. 2016), 5174–86.
- [8] E. Candes, X. Li, and M. Soltanolkotabi. “Phase Retrieval via Wirtinger Flow: Theory and Algorithms”. In: *IEEE Trans. Info. Theory* 61.4 (Apr. 2015), pp. 1985–2007.
- [9] R. W. Gerchberg and W. O. Saxton. “Practical Algorithm for Determination of Phase from Image and Diffraction Plane Pictures”. In: *OPTIK* 35.2 (1972), 237–246.
- [10] P. Thibault and M. Guizar-Sicairos. “Maximum-likelihood refinement for coherent diffractive imaging”. In: *New J. of Phys.* 14.6 (June 2012), p. 063004.
- [11] A. Goy, K. Arthur, S. Li, and G. Barbastathis. “Low photon count phase retrieval using deep learning”. In: *Phys. Rev. Lett.* 121.24 (Dec. 2018), p. 243902.
- [12] R. Xu, M. Soltanolkotabi, J. P. Haldar, W. Unglaub, J. Zusman, A. F. J. Levi, and R. M. Leahy. *Accelerated Wirtinger flow: A fast algorithm for ptychography*. 2018.
- [13] D. A. Barmherzig and J. Sun. “Low-photon holographic phase retrieval”. In: *OSA: Computational Optical Sensing and Imaging*. 2020.
- [14] I. Vazquez, I. E. Harmon, J. C. R. Luna, and M. Das. “Quantitative phase retrieval with low photon counts using an energy resolving quantum detector”. In: *J. Opt. Soc. Am. A* 38.1 (Jan. 2021), 71–9.
- [15] H. Lawrence, D. A. Barmherzig, H. Li, M. Eickenberg, and M. Gabriele. *Phase retrieval with holography and untrained priors: Tackling the challenges of low-photon nanoscale imaging*. 2020.
- [16] D. L. Snyder, C. W. Helstrom, A. D. Lanterman, M. Faisal, and R. L. White. “Compensation for readout noise in CCD images”. In: *J. Opt. Soc. Am. A* 12.2 (Feb. 1995), 272–83.
- [17] H. Zhang and D. P. Mandic. “Is a complex-valued stepsize advantageous in complex-valued gradient learning algorithms?” In: *IEEE Trans. Neural Net. Learn. Sys.* 27.12 (Dec. 2016), 2730–5.
- [18] K. Choi and A. D. Lanterman. “Phase retrieval from noisy data based on minimization of penalized I-divergence”. In: *J. Opt. Soc. Am. A* 24.1 (Jan. 2007), 34–49.
- [19] E. J. Candes, Y. C. Eldar, T. Strohmer, and V. Voroninski. “Phase retrieval via matrix completion”. In: *SIAM J. Imaging Sci.* 6.1 (2013), 199–225.
- [20] Y. Chen and E. J. Candes. “Solving random quadratic systems of equations is nearly as easy as solving linear systems”. In: *Comm. Pure Appl. Math.* 70.5 (May 2017), 822–83.
- [21] H. Chang and S. Marchesini. “Denoising Poisson phaseless measurements via orthogonal dictionary learning”. In: *Optics Express* 26.16 (Aug. 2018), 19773–96.
- [22] Y. Zhang, P. Song, and Q. Dai. “Fourier ptychographic microscopy using a generalized Anscombe transform approximation of the mixed Poisson-Gaussian likelihood”. In: *Optics Express* 25.1 (Jan. 2017), 168–79.
- [23] I. Kang, F. Zhang, and G. Barbastathis. “Phase extraction neural network (PhENN) with coherent modulation imaging (CMI) for phase retrieval at low photon counts”. In: *Optics Express* 28.15 (July 2020), 21578–600.
- [24] D. L. Snyder, A. M. Hammoud, and R. L. White. “Image recovery from data acquired with a charge-coupled-device camera”. In: *J. Opt. Soc. Am. A* 10.5 (May 1993), 1014–23.
- [25] D. Böhning and B. G. Lindsay. “Monotonicity of quadratic approximation algorithms”. In: *Ann. Inst. Stat. Math.* 40.4 (Dec. 1988), 641–63.
- [26] T. Qiu and D. P. Palomar. “Undersampled sparse phase retrieval via majorization-minimization”. In: *IEEE Trans. Sig. Proc.* 65.22 (Nov. 2017), 5957–69.
- [27] I. Daubechies, M. Debrise, and C. De Mol. “An iterative thresholding algorithm for linear inverse problems with a sparsity constraint”. In: *Comm. Pure Appl. Math.* 57.11 (Nov. 2004), 1413–57.
- [28] A. Beck and M. Teboulle. “A fast iterative shrinkage-thresholding algorithm for linear inverse problems”. In: *SIAM J. Imaging Sci.* 2.1 (2009), 183–202.
- [29] D. Kim and J. A. Fessler. “Adaptive restart of the optimized gradient method for convex optimization”. In: *J. Optim. Theory Appl.* 178.1 (July 2018), 240–63.
- [30] K. Lange. “A gradient algorithm locally equivalent to the EM Algorithm”. In: *J. Royal Stat. Soc. Ser. B* 57.2 (1995), 425–37.
- [31] D. R. Hunter and K. Lange. “A tutorial on MM algorithms”. In: *American Statistician* 58.1 (Feb. 2004), 30–7.
- [32] J. de Leeuw and K. Lange. “Sharp quadratic majorization in one dimension”. In: *Comp. Stat. Data Anal.* 53.7 (May 2009), 2471–84.
- [33] S. Boyd, N. Parikh, E. Chu, B. Peleato, and J. Eckstein. “Distributed Optimization and Statistical

- Learning via the Alternating Direction Method of Multipliers”. In: *Found. Trends Mach. Learn.* 3.1 (Jan. 2011), pp. 1–122.
- [34] Y. Wang, W. Yin, and J. Zeng. “Global convergence of ADMM in nonconvex nonsmooth optimization”. In: *J. Sci. Comp.* 78.1 (2019), 29–63.
- [35] T. Bendory, R. Beinert, and Y. C. Eldar. “Fourier Phase Retrieval: Uniqueness and Algorithms”. In: *Compressed Sensing and its Applications*. Applied and Numerical Harmonic Analysis. Springer Intl. Publishing, 2018, pp. 55–91.
- [36] Y. Shechtman, Y. C. Eldar, O. Cohen, H. N. Chapman, J. Miao, and M. Segev. “Phase Retrieval with Application to Optical Imaging: A contemporary overview”. In: *IEEE Sig. Proc. Mag.* 32.3 (2015), pp. 87–109.
- [37] R. Chandra, Z. Zhong, J. Hontz, V. McCulloch, C. Studer, and T. Goldstein. “PhasePack: A Phase Retrieval Library”. In: *Asil. Conf. Sig. Sys. Comp.* (2017), pp. 1617–1621.
- [38] C. A. Metzler, M. K. Sharma, S. Nagesh, R. G. Baraniuk, O. Cossairt, and A. Veeraraghavan. “Coherent inverse scattering via transmission matrices: Efficient phase retrieval algorithms and a public dataset”. In: *Proc. Intl. Conf. Comp. Photography*. 2017, 1–16.

## APPENDIX

### A. Proof of the improved curvature

This appendix proves that the curvature formula (18) provides a majorizer for the negative log-likelihood of the Poisson model that always is bounded above by the maximum curvature (7).

For Poisson phase retrieval, we drop the subscript  $i$  and irrelevant constants and focus on the negative log-likelihood for real case for simplicity:

$$h(r) = (r^2 + b) - y \log(r^2 + b), \quad (38)$$

where  $r \in \mathbb{R}, y \geq 0, b \geq 0$ .

One can generalize the majorizer derived here for (38) to the complex case by taking the magnitude and some other minor modifications.

First, we consider some simple cases:

- If  $y = 0$ , then (38) is a quadratic function, so no quadratic majorizer is needed.
- If  $b = 0$  and  $y > 0$  then (38) has unbounded 2nd derivative so no quadratic majorizer exists.

- If  $b = 0$  and  $r = 0$ , then  $y$  must be zero because a Poisson random variable with zero mean can only take the value 0. Thus again quadratic majorizer is not needed.

So hereafter, we assume that  $y > 0, b > 0$ . Under these assumptions, the derivatives of (38) are:

$$\dot{h}(r) = 2r \left( 1 - \frac{y}{r^2 + b} \right) \quad (39)$$

$$\ddot{h}(r) = 2 + 2y \frac{r^2 - b}{(r^2 + b)^2} \quad (40)$$

$$h^{(3)}(r) = \frac{2yr(3b - r^2)}{(r^2 + b)^3}, \quad (41)$$

where  $h^{(3)}(r)$  denotes the third derivative. Clearly,  $\dot{h}(r)$  is convex on  $(-\infty, -\sqrt{3b}]$  and  $[0, \sqrt{3b}]$ , and concave on  $[-\sqrt{3b}, 0]$  and  $[\sqrt{3b}, +\infty)$ , based on the sign of  $h^{(3)}(r)$ .

A quadratic majorizer of  $h$  at point  $s$  has the form:

$$H(r; s) = h(s) + \dot{h}(s)(r - s) + \frac{1}{2}c(s)(r - s)^2. \quad (42)$$

The derivative of this function (w.r.t.  $r$ ) is:

$$\dot{H}(r; s) = c(s)(r - s) + \dot{h}(s). \quad (43)$$

By design, this kind of quadratic majorizer satisfies  $H(s; s) = h(s)$  and  $\dot{H}(s; s) = \dot{h}(s)$ . The only thing we need is to pick  $c(s)$  and we want it to be as small as possible subject to the majorization requirement  $H(r; s) \geq h(r), \forall r$ , yet we also want  $c(s)$  to be easy to compute. From (41), we note that  $r^2 = 3b$  is a maximizer of  $\ddot{h}$  so the maximum curvature is:

$$\ddot{h}(r) \leq 2y \frac{2b}{(4b)^2} + 2 = 2 + \frac{y}{4b}. \quad (44)$$

**Proposition:**  $H(r; s)$  defined in (42) is a majorizer of  $h(r)$  when  $c(s) = c_{\text{imp}}(s)$ , where:

$$c_{\text{imp}}(s) \triangleq \begin{cases} \ddot{h}(g(s)), & s \neq 0, \\ \lim_{s \rightarrow 0} \ddot{h}(g(s)), & s = 0, \end{cases} \quad (45)$$

where

$$g(s) \triangleq \frac{b + \sqrt{b^2 + bs^2}}{s}. \quad (46)$$

By construction, the proposed curvature  $c(s)$  is at most the max curvature given in (44).

**Proof:** Because of the symmetry of  $\ddot{h}(r)$ , it suffices to prove the proposition for  $s \geq 0$  without loss of generality. First we consider some trivial cases:

- 1) If  $s = 0$ , one can verify  $\lim_{s \rightarrow 0} \ddot{h}(g(s)) = 2$ . In

this case,  $H(r; s)$  is simply

$$\begin{aligned} H(r; 0) &= h(0) + \frac{1}{2}c(0)r^2 \\ &= r^2 + b - y \log(b) \\ &\geq r^2 + b - y \log(r^2 + b) = h(r). \end{aligned} \quad (47)$$

2) If  $s = \sqrt{3b}$ , one can verify

$$\ddot{h}(g(\sqrt{3b})) = 2 + \frac{y}{4b}. \quad (48)$$

So in this case  $\ddot{h}(g(s))$  equals the maximum curvature.

Hereafter, we consider only  $s > 0$  and  $s \neq \sqrt{3b}$ , so it suffices to prove that

$$\begin{aligned} \forall r \in (-\infty, s], \quad \dot{h}(r) &\geq \dot{H}(r; s), \\ \forall r \in [s, +\infty), \quad \dot{h}(r) &\leq \dot{H}(r; s), \end{aligned} \quad (49)$$

because if (49) holds, then  $\forall \tilde{r} < s$ :

$$\begin{aligned} H(s; s) - H(\tilde{r}; s) &= \int_{\tilde{r}}^s \dot{H}(r; s) dr \\ &\leq \int_{\tilde{r}}^s \dot{h}(r) dr = h(s) - h(\tilde{r}), \end{aligned} \quad (50)$$

and  $\forall \tilde{r} > s$ :

$$\begin{aligned} H(\tilde{r}; s) - H(s; s) &= \int_s^{\tilde{r}} \dot{H}(r; s) dr \\ &\geq \int_s^{\tilde{r}} \dot{h}(r) dr = h(\tilde{r}) - h(s). \end{aligned} \quad (51)$$

Together with  $H(s; s) = h(s)$ , we will have shown  $H(r; s) \geq h(r)$ ,  $\forall r \in \mathbb{R}$  after showing (49).

Substituting  $\dot{H}(r; s) = c(s)(r-s) + \dot{h}(s)$ , one can verify that showing (49) simplifies to showing

$$c_{\text{imp}}(s) \geq \frac{\dot{h}(r) - \dot{h}(s)}{r - s}, \quad \forall r \in \mathbb{R}, r \neq s. \quad (52)$$

Furthermore, when  $s > 0$ , the parabola  $H(\cdot; s)$  is symmetric about its minimizer:

$$\begin{aligned} a &= a(s) \triangleq \underset{r}{\operatorname{argmin}} H(r; s) = s - \frac{\dot{h}(s)}{c_{\text{imp}}(s)} \\ &= \frac{s \ddot{h}(g(s)) - \dot{h}(s)}{\ddot{h}(g(s))} \geq 0. \end{aligned} \quad (53)$$

This minimizer is nonnegative because  $\dot{h}(s) \leq 2s$  and

$$\begin{aligned} c_{\text{imp}}(s) &= \ddot{h}(g(s)) = 2 + \frac{ys^2(b + \sqrt{b^2 + bs^2})}{b(b + s^2 + \sqrt{b^2 + bs^2})^2} \\ &\geq 2. \end{aligned} \quad (54)$$

Thus, if  $h(r) \leq H(r; s)$  when  $r \geq 0$ , we have  $h(-r) = h(r) \leq H(r; s) \leq H(-r; s) = H(r + 2a; s)$ , so it

suffices to prove (52) only for  $r \geq 0$ , which simplifies (52) to showing

$$c_{\text{imp}}(s) \geq \frac{\dot{h}(r) - \dot{h}(s)}{r - s}, \quad \forall r \geq 0, r \neq s. \quad (55)$$

In short, if (55) holds, then  $H(r; s) \geq h(r)$ ,  $\forall r \in \mathbb{R}$ .

To prove (55), we first exploit a useful property of  $c_{\text{imp}}(s)$ . The intuition behind  $c_{\text{imp}}(s)$  is that the affine function connecting points  $(g(s), \dot{h}(g(s)))$  and  $(s, \dot{h}(s))$  is tangent to  $\dot{h}(r)$  at point  $r = g(s)$ , so that one can verify

$$\ddot{h}(g(s)) = c_{\text{imp}}(s) = \frac{\dot{h}(g(s)) - \dot{h}(s)}{g(s) - s}, \quad g(s) \neq s. \quad (56)$$

Moreover, one can verify  $g(s) = s$  implies  $s = \sqrt{3b}$  for  $s > 0$ , so (56) is valid by our assumption above ( $s > 0$  and  $s \neq \sqrt{3b}$ ). Fig. 9 visualizes this tangent property.

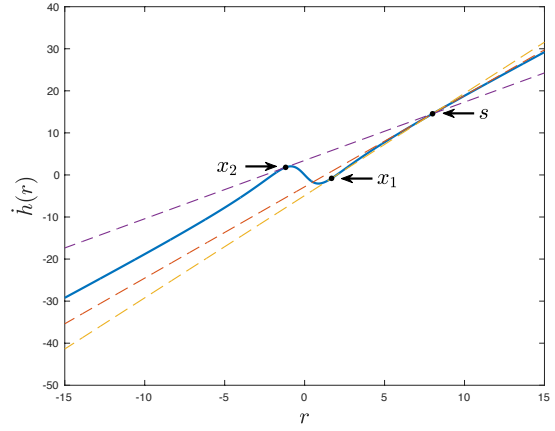


Fig. 9: Visualization of tangent property where  $s = 8$ ,  $y = 6$ ,  $b = 2$ . The blue curve is  $\dot{h}(r)$ , and the dashed lines are tangent to  $\dot{h}(r)$  at  $x_1 = g(s) = (b + \sqrt{b^2 + bs^2})/s$ ,  $x_2 = (b - \sqrt{b^2 + bs^2})/s$  and  $s$ .

Let  $f(r) = (\dot{h}(r) - \dot{h}(s))/(r - s)$ , where  $r \geq 0$  and  $r \neq s$ , plugging in  $\dot{h}(r)$  and  $\dot{h}(s)$  yields:

$$f(r) = 2 + \frac{2y(sr - b)}{(s^2 + b)(r^2 + b)}. \quad (57)$$

Differentiating w.r.t.  $r$  leads to:

$$\dot{f}(r) = \frac{2y}{s^2 + b} \cdot \frac{-sr^2 + 2br + bs}{(r^2 + b)^2}, \quad (58)$$

where one can verify the positive root of  $-sr^2 + 2br + bs = 0$  is  $g(s)$ . Together with  $\dot{f}(r) > 0$  when  $r \in (0, g(s))$  and  $\dot{f}(r) < 0$  when  $r \in (g(s), \infty)$ , we have that (55) holds because  $f(r)$  achieves its maximum at  $f(g(s))$ :

$$f(r) \leq f(g(s)) = c_{\text{imp}}(s). \quad \blacksquare \quad (59)$$

SUPPLEMENTAL MATERIALS  
FOR  
ALGORITHMS FOR POISSON PHASE RETRIEVAL  
Z. LI, K. LANGE, J. FESSLER

*Illustration of the improved curvature*

Although the optimal curvature might not be computed easily, we can mathematically express the optimal curvature as [32]:

$$c_{\text{opt}}(s) = \sup_{r \neq s} \frac{2(h(r) - h(s) - \dot{h}(s)(r - s))}{(r - s)^2}, \quad (\text{S.1})$$

where one can verify  $c_{\text{imp}}$  is close to  $c_{\text{opt}}$  if the supremum is achieved near  $s$ . Letting  $t = r - s$ , one can empirically find  $c_{\text{opt}}(s)$  by searching all possible  $t$  for any  $s$ . For the following plots, we search from  $t = -1000 : 0.0011 : 1000$  for all  $s = -20 : 0.009 : 20$ .

Fig. S.1 shows that the proposed curvature lies between the maximum curvature and the optimal curvature (found empirically). From these plots, we can see that when  $s$  is near zero, the proposed curvature and the optimal curvature are close. These plots partially illustrate the near optimality of  $c_{\text{imp}}$  when  $s$  is near zero but there still remains space for improvement when  $|s|$  is large.

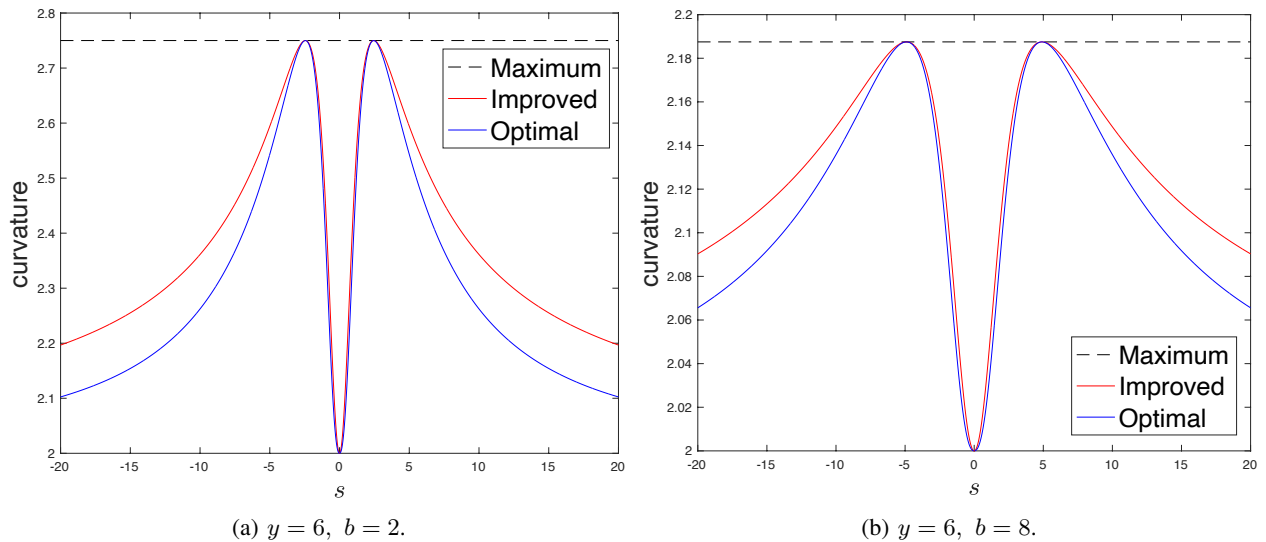


Fig. S.1: Plot of proposed curvature and max and optimal curvature, for the case  $y = 6, b = 2$  and  $y = 6, b = 8$ , respectively.

### Computation time comparison

Fig. S.2 compares the convergence rates of the Poisson phase retrieval algorithms in the case where the number of unknowns  $N$  is small enough that both backsubstitution (BS) (backslash in Julia) and CG are viable options for solving the inner quadratic optimization problems. In every case the CG version of 250 iterations decreased NRMSE faster than the BS version.

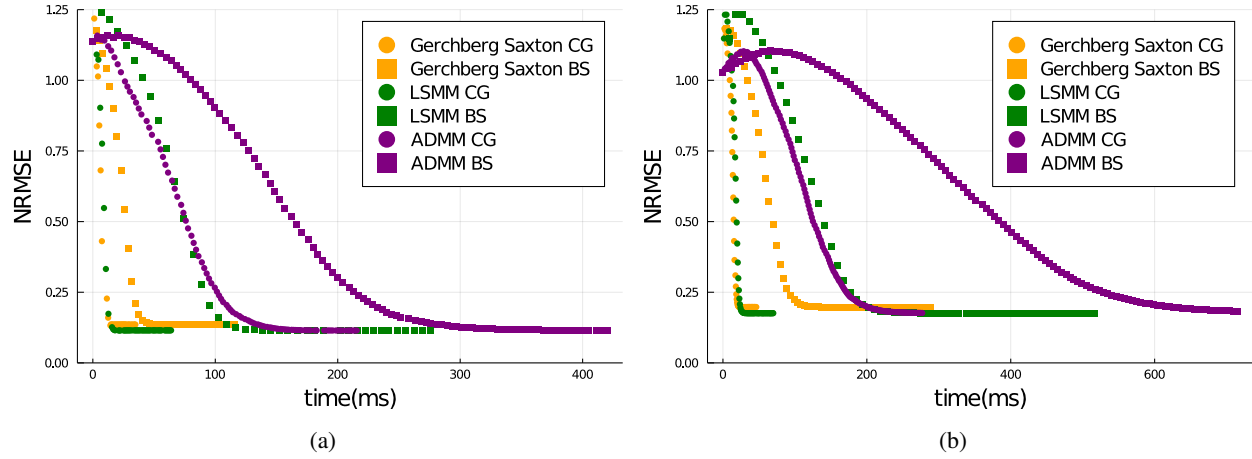


Fig. S.2: NRMSE vs. time (ms) using different update strategy, where CG denotes conjugate gradient and BS denotes back slash in Julia to solve least square problems. Here  $\mathbf{A}$  is random Gaussian with the average of  $\mathbf{a}'_i \mathbf{x}$  equals to 2,  $M = 3000$  and  $b_i = 0.5$ . Subfigure (a) and (b) correspond to  $\mathbf{x}_{\text{true-A}}$  and  $\mathbf{x}_{\text{true-B}}$ , respectively.